Proteins: Structure, Function, and Bioinformatics

WILEY

PROTEINS

RESEARCH ARTICLE OPEN ACCESS

Structural Modeling and Dynamics of the Full-Length Homer1 Multimer

Zsófia E. Kálmán[1] | András Czajlik[2] | Brigitta Maruzs[1] | Fanni Farkas[1] | István Pap[1] | Csilla Homonnay[1] | Tomas Klumpler[3] | Gyula Batta[4] | Zoltán Gáspári[1] | Bálint Péterfia[1]

[1]Faculty of Information Technology and Bionics, Pázmány Péter Catholic University, Budapest, Hungary | [2]Department of Biochemistry, Semmelweis University, Budapest, Hungary | [3]CEITEC Masaryk University, Brno, Czech Republic | [4]Department of Organic Chemistry, University of Debrecen, Debrecen, Hungary

Correspondence: Bálint Péterfia (peterfia.balint.ferenc@itk.ppke.hu)

Received: 10 June 2025 | **Revised:** 3 November 2025 | **Accepted:** 12 November 2025

Keywords: coiled coil | dynamics | EVH1 domain | MD simulation | NMR

ABSTRACT

Homer proteins are modular scaffold molecules that constitute an integral part of the protein network within the postsynaptic density. Full-length Homer1 forms a large homotetramer via a long coiled coil region, and can interact with proline-rich target sequences with its globular EVH1 domain. Here we report an atomistic model of the Homer1 coiled coil region along with the NMR solution structure and backbone dynamics of its EVH1 domain, with implications for the organization of the full-length tetramer. Compared to the already available EVH1 structures, our NMR ensemble exhibits subtle differences, mostly in and around its partner binding region, suggesting the presence of ligand-induced conformational transitions. Molecular dynamics simulations of the long coiled coil reveal distinct regions with different stability and flexibility, with the N-terminal part of the coiled coil exhibiting the largest motions. Interestingly, this segment is highly conserved, pointing to the functional relevance of the observed dynamical features. Our results indicate previously unexplored aspects of the flexibility of the full-length Homer1 tetramer that might contribute to the dynamic rearrangements of the postsynaptic protein network linked to its functional transitions.

1 | Introduction

Excitatory synapses contain a highly organized network of different proteins. Beneath the postsynaptic membrane, a pronounced structure, called the postsynaptic density (PSD), is located [1], which is primarily organized by large multivalent scaffold proteins [2]. The three members of the Homer family (named Homer1, Homer2, and Homer3) are among the major scaffolding proteins in mammals [3] and Homer1 has several splice variants with different domain organization. The shortest isoform (Homer1a) contains only the N-terminal EVH1 domain and a short, disordered C-terminus, while the longer forms (Homer1b and Homer1c) both harbor the EVH1 domain connected to a long C-terminal coiled coil segment by a long disordered hinge region [4, 5]. The coiled coil segment mediates higher-order assembly of multiple Homer polypeptide chains. Hayashi and colleagues proposed a model where the long coiled coil region is divided into two segments: the first is a short, dimeric, parallel coiled coil, and a second starting as a parallel dimer continued as a tetramer by interconnecting the dimeric C-terminals in an antiparallel orientation [6] (Figure S1).

The highly conserved EVH1 domain belongs to the Class I type EVH1 domain that binds proline-rich short linear motifs (SLiMs) with the consensus sequences FPxoP and PPxxF (where x is any residue and o stands for hydrophobic residues) [7]. Most of the Homer interaction partners characterized so far bind to the EVH1 domain [8]. Multiple membrane receptors such as mGluR5 and

Zsófia E. Kálmán and András Czajlik have equal contribution to the work.

IP3 receptors are linked to the deeper layer of the PSD through their interaction with Homer [9]. It also forms complexes with ion channels and transmembrane proteins such as TRPC1 [10]. Homer forms a mesh-like structure with Shank proteins and via this interaction it is also linked to the major scaffold protein, GKAP [6]. In addition, Homer1 is anchored to the cytoskeleton through the connection with drebrin and F-actin [4, 8]. It was also discovered that Homer contains an internal sequence SPLTP, called the P-motif, in the long hinge region between the EVH1 domain and the coiled coil segment. This motif has been suggested to form weak interactions with the EVH1 domain, although this has been observed only in the crystal state and not in solution; therefore the physiological relevance of this interaction is not yet clear [3].

Homer plays an essential role in determining the shape and density of the synapse, expected to be closely associated with the fundamental molecular mechanisms behind learning and memory. The presence of Homer1 isoforms seems to be tightly regulated as the short Homer1a isoform acts as a negative regulator blocking the formation of higher-order complexes of the larger, tetrameric isoforms. Homer1 is also a key protein in the reorganization of the PSD during sleep, when the monomeric Homer1a isoform gets dominant over the larger tetrameric assembly and thus disrupts the direct connections between mGluR5 receptor subunits in the postsynaptic membrane and the IP3 receptors in the ER [9]. The dysfunction of Homer proteins was also linked to many neurological symptoms; Homer is believed to play a role in schizophrenia, Fragile X syndrome and many more [8].

In this work we describe a structural model of the full-length Homer1c isoform by combining the globular, intrinsically disordered and coiled coil segments into multimeric structures. This is a prerequisite to include the protein in larger, more complex models of postsynaptic protein assemblies to understand the organization of the PSD at a larger scale. A key aspect is to describe the local and global flexibility of the protein. To this end, we have determined the solution structure and dynamics of the EVH1 domain by NMR spectroscopy and have performed molecular dynamics simulations on the dimeric and tetrameric complexes of Homer.

For the modeling, we chose the sequence of rat Homer1. The reason for this is that the experimentally determined structure of the tetrameric coiled coil region is available for this species, and this choice does not affect the EVH1 domain as its sequence is 100% identical between the human, mouse and rat proteins. In order to assess the stability of different regions of the coiled coil, we used a simplified, dimeric model derived from the full tetramer, assuming that the identical dimeric parts behave similarly. The emerging picture is that of a highly dynamic assembly that can span a large variety of distances and link partners at versatile mutual locations and orientations.

2 | Materials and Methods

2.1 | Cloning, Protein Expression and Purification

Mus musculus Homer1 EVH1 domain coding insert was ligated into the Nde1 and BamH1 restriction sites of a modified pET-15b plasmid backbone (Novagen)– that contains an N-terminal 6xHis-tag and a tobacco etch virus (TEV) protease cleavage site. The expressed protein corresponds to UniProt Q9Z2Y3, 1-118 sequence: gshMGEQPIFSTRAHVFQIDPNTKKNWVPTSKHAVTVSYFYDSTRNVYRIISLDGSKAIINSTITPNMTFTKTSQKFGQWADSRANTVYGLGFSSEHHLSKFAEKFQEFKEAARLAKEKSQ where the first 3 amino acids remain after cleavage of the expression tag. Note that murine and human sequences are identical at this section of the Homer1 protein. The recombinant protein was expressed in BL21 (DE3) *Escherichia coli* bacterial cells (Novagen) for 20 h incubation at 20°C with 150 rpm shaking after induction with 1 mM IPTG (isopropyl β-D-1-thiogalactopyranoside) (Sigma) at a cell density of 4 MFU. After centrifugation, the cell pellets were stored at −20°C until further use. Unlabeled EVH1 protein was expressed in cells grown in LB medium. For isotopically labeled (^{15}N and ^{15}N, ^{13}C) protein production M9 medium was used [11] supplemented with 0.2× Trace element mix [12], 2.5 g/L $^{15}NH_4Cl$ (Cambridge Isotope Laboratories, Cambridge, MA), and 4 g/L unlabeled glucose or [^{13}C]-D-glucose in the case of the double-labeled version. Harvested cells were disrupted by sonication in a 10% suspension of lysis buffer (300 mM NaCl, 50 mM sodium phosphate, pH 7.4) using an ultrasonic homogenizer (BioLogics). Homer EVH1 proteins were purified from the supernatant after homogenization with a 5 mL Bio-Scale Nuvia IMAC Ni-affinity column (Bio-Rad) equilibrated with binding buffer (50 mM sodium phosphate, 300 mM NaCl, pH 7.4). This binding buffer was also used for washing and elution steps, supplemented with 50 mM and 250 mM of imidazole, respectively. IMAC purification was followed by His-tag cleavage with TEV protease (25 μg TEV/g EVH1, 10°C, ON). After TEV treatment, the buffer was exchanged to low salt phosphate buffer (binding buffer with 20 mM NaCl) using HiTrap desalting columns with Sephadex G-25 resin (Cytiva), and the sample was further purified by ion exchange chromatography, using a Bio-Scale Mini Macro-Prep High S column. Gradient elution was performed by adding NaCl to the binding buffer up to 500 mM. Reverse IMAC was applied to get rid of the cleaved His-tag and the TEV enzyme. In the case of samples for NMR measurement an additional SEC (size exclusion chromatography) step was included using a SEC70 analytical gel chromatography column (Bio-Rad). Before and after SEC, the sample was concentrated with the Amicon Ultra 15 mL Centrifugal Filter unit with 3 kDa MWCO. The recombinant EVH1 protein was eluted in low salt sodium phosphate buffer (50 mM sodium phosphate; 20 mM NaCl, 0.02% NaN_3; pH 7.4). To determine its purity and molecular weight, SDS-PAGE (sodium dodecyl sulfate–polyacrylamide gel electrophoresis) was applied, and the concentration was measured by determining A280 using a NanoDrop2000 instrument and the extinction coefficient estimated from the protein sequence by a protein calculator software (https://protcalc.sourceforge.net/).

2.2 | Far-UV CD Spectroscopy

Far-UV CD spectroscopy measurement was performed using a JASCO J-1500 CD spectrometer (JASCO Corporation, Tokyo, Japan) in the 195–250 nm spectral range, 50 nm/min scanning speed, 1 nm bandwidth, 0.2 nm step size, 0.5 s response time and 3 scans of accumulation and baseline correction. It was recorded in a 1 mm pathlength quartz cuvette (J/21, Jasco). Sample concentrations were 10 μM in 50 mM Sodium Phosphate Buffer, 20 mM NaCl, pH 7.4 buffer. In order to check temperature

dependence, the 20°C–60°C interval was used; measurement was done in every tenth degree.

Secondary structure calculation and data evaluation were performed with BeStSel (https://bestsel.elte.hu) [13].

2.3 | Mass Spectrometry

To determine the exact molecular weight, mass spectrometry measurements were performed on the TEV-treated H118 protein. HPLC–MS measurements of the proteins were performed using a Shimadzu LC-MS-2020 device with a Reprospher-100 C18 column and a positive–negative double ion source (DUIS±) with a quadrupole MS analyzer in a range of m/z 50–1000. Gradient elution was applied using eluent A (0.1% formic acid in water) and eluent B (0.1% formic acid in acetonitrile). According to the MS results, the efficiency of isotopic labeling was found to be 98% for ^{15}N and 97% for ^{13}C labelling.

2.4 | NMR Measurement Conditions and Data Analysis

For data collection, samples of 600 μL containing 190 μM ^{13}C, ^{15}N-labeled protein in a solution of 50 mM Sodium Phosphate Buffer, 20 mM NaCl, 0.02% NaN_3 at pH 7.36 were prepared. Measurements were performed on a Bruker Avance NEO 700 MHz spectrometer at 298 K. For resonance assignment, standard 2D (^1H-^{15}N HSQC and ^1H-^{13}C HSQC) and 3D triple-resonance (HNCA, HN(CO)CA HNCACB, HN(CO)CACB, HNCO, HN(CA)CO, HCCONH, HCCH-TOCSY) and HBCBCGCDHD spectra were acquired. To aid structure determination, 2D NOESY, 3D TOCSY-HSQC, and NOESY-HSQC spectra were also recorded.

Initial structure calculation was performed with the ATNOS/CANDID/Cyana [14] suite using 7 cycles. For the calculation, NOE restraints along with TALOSN-based [15] dihedral angle restraints (for 99 phi and 97 psi angles) were used. To improve local geometry, the 20 best structures obtained were further refined with XPLOR-NIH version 3.9 [16], with the default force field without any solvent model and using the NOE restraints only, that is, without the dihedral restraints. For this, the protocol "Refine.py," applicable when a good initial model is available, was slightly modified to use a gentle simulated annealing protocol with an upper temperature of 150°C to preserve the input conformations while allowing optimization of the local geometry. Before refinement, NOE restraints were manually curated to exclude any remaining non-trivial redundancies like both specific and ambiguous inclusion of geminal protons in separate restraints to the same partner atoms. The stereospecific restraints deduced by the initial protocol were retained, and atom names were converted between the Cyana [14] and XPLOR [16] formats with in-house scripts. As the initial ATNOS/CANDIS/Cyana protocol uses the so-called sum averaging method, the restraints were rescaled and binned to be suitable for the simple distance averaging setting used in our XPLOR-NIH refinement step.

Validation was performed using the standard RCSB Validation service as well as PSVS version 1.5 [17]. Visualization of the structure was performed using MOLMOL [18] and Chimera [19]. Electrostatic surface calculation was performed using ABPS as available through the site https://server.poissonboltzmann.org/ [20].

Using the same sample as for the structure determination, backbone ^{15}N relaxation measurements were performed at 700 MHz (^{15}N frequency 70.95 MHz) using standard Bruker pulse sequences in pseudo3D format using delay times of 40, 80, 120, 160, 200, 300, 400, 600, 1200, and 2400 ms for T_1 and 1, 2, 3, 4, 5, 6, 7, 9,12, 15, and 18 cycles of a 16.96 ms loop (calculated from parameters p30 and d21 in the Bruker pulse sequence) for T_2 measurements. ^1H-^{15}N heteronuclear NOE was measured in an interleaved fashion with a delay time of 7 s. Spectra were processed with TopSpin and analyzed with NMRFAM-Sparky 1.413 [21], including intensity calculation and curve fitting. Model-free analysis was performed with Tensor2 [22]. Tensor2 uses a ^{15}N chemical shift anisotropy (CSA) value of −170 ppm, and we used the default angle of 0° between the dipolar interaction and the CSA. We performed several exploratory calculations with different settings to estimate the robustness of the results. Peaks with severe overlap were excluded from the final calculations. For the estimation of the rotational correlation time, data only for residues with T_1/T_2 values within 1 standard deviation of the average (calculated from non-overlapping peaks) were used. The isotropic diffusion model was chosen as considering an anisotropic tensor did not provide significant improvement over it. Residues with unreliable model-free calculation results, mostly because of hetNOE values above 1, were discarded from further analysis.

2.5 | Small Angle X-Ray Scattering Measurements

For SAXS measurements, the sample preparation protocol was similar to the above-mentioned NMR sample preparation. The only difference was that unlabeled proteins were used. SAXS data was collected from 8, 4, 2, and 1 mg/mL (approximately 0.58, 0.29, 0.15, and 0.07 mM, respectively) protein samples.

SAXS data was collected using a Rigaku BioSAXS-2000 instrument at CEITEC (Brno, Czech Republic) equipped with a HyPix-3000 detector at a sample-detector distance of 0.48 m. Scattered intensity was measured in the range 0.008–0.65 1/Å, where $q = 4\pi \sin\theta/\lambda$; 2θ is the scattering angle and $\lambda = 0.154$ nm. Six 10 min frames were collected at a sample temperature of 25°C. The data were normalized to the intensity of the transmitted beam and radially averaged. Scattering curves from individual frames were checked for radiation damage and averaged. The corresponding scattering from the solvent-blank was subtracted to produce the scattering profile.

Structure-based calculation of SAXS curves was performed with Pepsi-SAXS [23]. The curves for the 20 individual conformers were averaged.

2.6 | Model Building and MD Simulations

For the Homer tetramer modeling, the solved rat crystal structures covering the protein terminals (PDB IDs: 1ddv [24] for the

N-terminal EVH1 domain and 3cve [6] for the C-terminal tetrameric coiled coil (CC)) were complemented by building the intermediate regions. The disordered-CC boundary was defined using MobiDB [25]. The characteristic coiled coil parameters such as radius and pitch were determined to match the geometry of the structure 3cve using CCBuilder [26]. Adjustment of the two parameters was done with a script using Ismabard [27]. Each generated dimeric parallel coiled coil was aligned to the structure 3cve using Chimera [19] (for chainA and chainB). After achieving the best model, we judged the inspection of the orientation of the N-terminals. The same process was repeated for the other half of the tetramer. After that, disordered segments were first modeled using Dipend [28] firstly creating a shorter version of the disordered segment [23]. With the help of the generated disordered segments, the EVH1 domain and the coiled coil segments were aligned together—then the disordered segment was removed. For the full-length disordered segment missing residues were modeled back using Modeler in Chimera [19]. The structure was tested with SOCKET [29] and minimized using FoldX [30] before molecular dynamics simulations. With this pipeline, we obtained the tetrameric structure from which we derived the dimeric form (removed chains), that was used separately in the majority of our investigations.

Computations were performed on the Komondor supercomputer. The models were simulated with GROMACS [31] using explicit solvent classical MD. The AMBER99SB-ILDN protein force field was used; the box setting was a minimum distance of 1.0 nm from the box edge. For the initial model five parallel 200 ns runs for the dimers were carried out (md_200_1, md_200_2, md_200_3, md_200_4, and md_200_5) from which snapshots were taken with a 10 ps frequency. Altogether, 20 000 models/run were generated from the trajectories.

For further analysis we used different tools. Secondary structure was predicted using DSSP [32]. From the DSSP predictions we also calculated the relative surface accessible area. SOCKET [29] was used to assign coiled-coil regions and heptad positions to the structures. Structures were visualized using Chimera [19]. We both used ColabFold [33] and AlphaFold3 [34] for the additional modeling tasks. Cα-Cα distances and salt bridges were calculated with in-house Perl and Python scripts. Matplotlib and Gnuplot were used for visualization. Sequence alignment was carried out using Jalview [35]. Vertebrate orthologous sequences were downloaded from OMA [36] and Shannon entropy was calculated with an in-house script.

3 | Results

3.1 | Expression of the Murine Homer1 EVH1 Construct

To characterize the EVH1 domain, the segment 1–118 from *M. musculus* Homer1 (UniProt ID: Q9Z2Y3) was selected (Figure 1A). Murine, rat and human sequences are 100% identical at this region of the Homer1 protein (Figure S2). The molecular weight (MW) of the unlabelled EVH1 domain was calculated to be 13.7 kDa (13736.38 Da) based on the encoded amino acid sequence. Mass spectrometry (MS) measurements confirmed that the correct sample was produced (13718.37 Da) and SDS – polyacrylamide gel electrophoresis (SDS – PAGE) also supports this result (Figure S3). Far-UV CD spectroscopy analysis of the successfully expressed Homer1 EVH1 domain in 50 mM Sodium Phosphate Buffer, 20 mM NaCl at pH 7.4 was consistent with an intact globular structure dominated by β-sheets (Figure 1B). BestSel [13] analysis indicates 13.6% alpha-helix, 46.3% beta-sheet and 40.1% non-classified secondary structure elements. Temperature-dependent CD measurements do not indicate major structural changes between 25°C and 60°C. Thus, the expressed EVH1 domain has a well-defined, stable structure (Figure 1B).

3.2 | Solution Structure of the EVH1 Domain

The ^{1}H-^{15}N HSQC spectrum of the EVH1 construct reveals a well-folded structure, characterized by high signal dispersion and predominantly well-resolved peaks. Complete backbone and partial sidechain NMR chemical shift assignments of the EVH1 1-118 domain were obtained. For the backbone, 99% of N, 95% of H and 99% of C atoms were assigned, whereas for the side chains, 86% of C and 88% of H atoms could be assigned. Chemical shifts have been deposited in BMRB under ID 34990 and the coordinates in the Protein Data Bank under ID 9QUX (Figure S4, Table 1). Table 1 reports the structure statistics of the structure along with the distance restraints used in the final refinement step.

The solution structure of the domain exhibits high overall similarity to the other available EVH1 structures, forming part of the larger PH domain family [7]. Throughout the text, we will use residue numbering matching the UniProt sequence (Q9Z2Y3), relative to which the numbering in the PDB entry is shifted by three residues because of the presence of the N-terminal expression tag. The structure matches the previously described EVH1 fold described in the literature as a β-sandwich [7] formed by seven strands, flanked by a long C-terminal α-helix. The first β-strand (strand A) is largely bent, its N-terminal region pairs with strand B, whereas its C-terminal part with strand G, therefore, the general fold, characteristic of the larger PH domain family, is also sometimes described as a β-barrel [37], although the strands are not without exposed hydrogen-bonding edges [38]. In the solution structure of Homer1 EVH1, the seven β-strands are formed by residues 8–15, 32–39, 44–51, 54–60, 67–71, 74–79, and 84–89, as identified by DSSPcont [39] (Figures 1C and S5). Most of the consecutive strands are linked by short turns, and even the longer, more irregular intra-strand segments 16–31 and 61–66 contain turn regions identified by DSSPcont. Residues 90–92, linking the last β-strand to the α-helix form a bend. The α-helix extends from residue 93 to 115, thus, only the last three residues at the C-terminus of the construct do not adopt helical conformation (Table S1). All buried amide NH groups participate in hydrogen bonds. SAXS measurements are in good agreement with the calculated structure, with a χ^2 of 1.067 between the experimental and the averaged back-calculated curve for the 20 conformers (Figure 1D). The SAXS data were deposited at SASBDB under the accession code SASDXK2.

The upfield ^{1}H chemical shifts of the sidechain atoms of Lys102 (Lys105 in the PDB entry) are indicative of the proximity of an

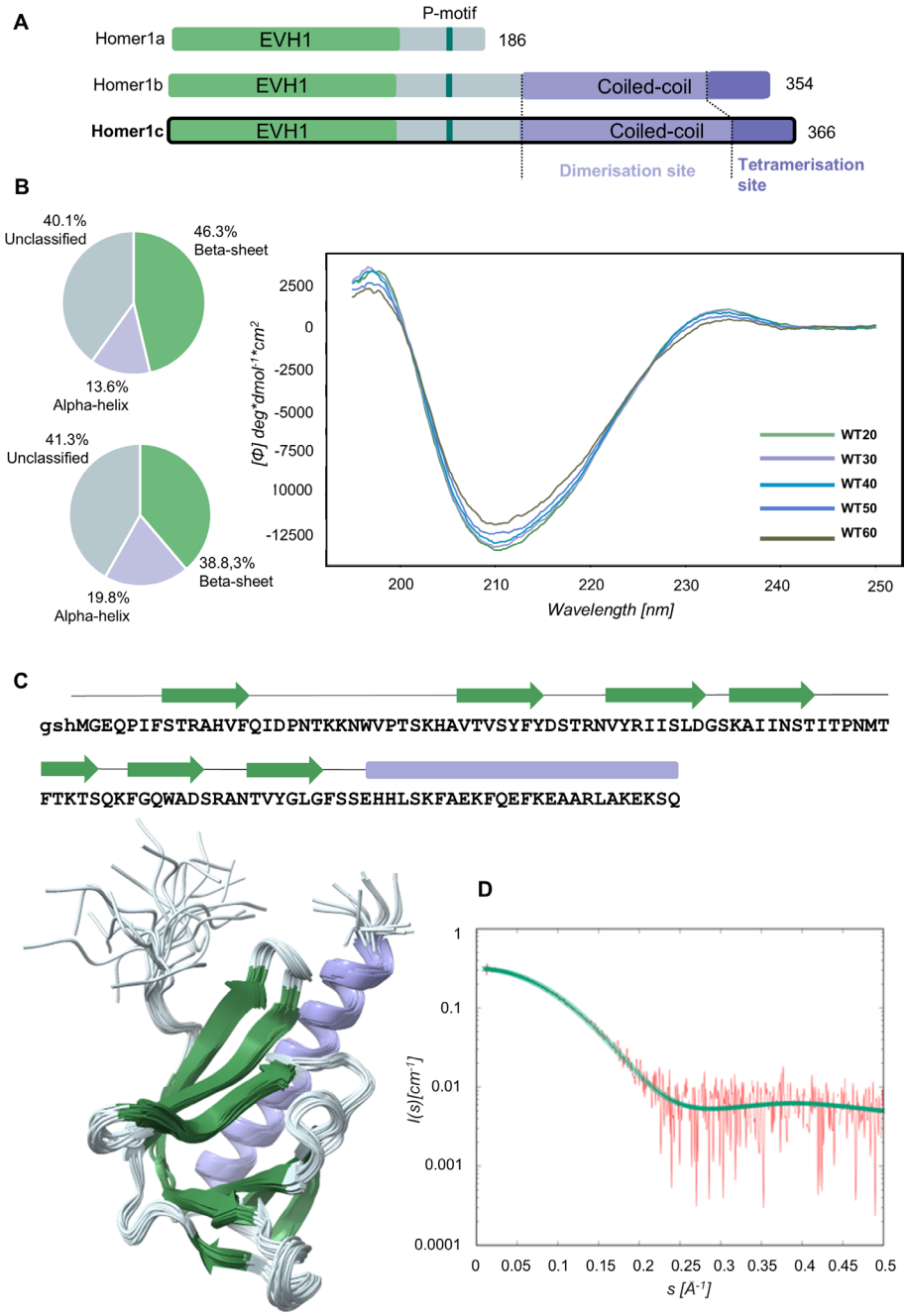

FIGURE 1 | General features of the EVH1 domain. (A) EVH1 domain of the Homer1c isoform was investigated in this study (B) Beta-sheet dominated globular structure of the EVH1 domain. CD spectra of the EVH1 domain construct. Secondary structure percentages calculated from the CD spectra using BestSel (upper diagram) from the average structure using DSSP (bottom diagram). (C) Position of the secondary structural elements in the sequence and in the structure. Green: beta-sheet, purple: alpha-helix, gray: Linkers and loops. The N-terminal 3 residues corresponding to the remnant of the expression tag are shown in lowercase. (D) Comparison of the measured (red) SAXS curve and the one calculated and averaged for the 20 conformers.

aromatic ring, consistent with the calculated structure where this residue is surrounded by the side chains of Phe7, Tyr36, Phe99 and Phe106 (Figure 2A). Phe99, Lys102 and Phe106 are located in the long α-helix, whereas Phe7 and Phe36 are in β-strands 1 and 2, respectively. Thus, this cation–π interaction links the C-terminal helix to the first half of the β-sheet. It can be noted that in our solution structure, the orientation of Lys102 is different from that observable in the Homer1 EVH1 x-ray structures, its side chain being closer to the aromatic rings in the NMR ensemble.

The electrostatic surface of the EVH1 domain is predominantly positive, with two regions with high positive charge. The first one (patch 1) is located between the first β-strand and the N-terminus of the helix, close to the ligand-binding site, and the second (patch 2) between the C-terminal segment of the helix and the tip of the β-barrel (Figure 2B).

Compared with other available Homer EVH1 structures (1ddv, 1ddw, 1i2h, 1i7a, 2p8v, 5zz9 [3, 24, 40–42]), the largest difference can be observed in the loop regions between residues 17–29 and

TABLE 1 | Summary of the solution structure of the Homer1 EVH1 domain.

Completeness of resonance assignments (%)		Model quality[a]	
Backbone	96	RMSD backbone[b] (Å)	0.3
Side chain	85	RMSD backbone (all residues, Å)	1.5
Aromatic	74	RMSD heavy atoms[b] (Å)	0.7
Stereospecific methyl	0	RMSD heavy atoms (all residues, Å)	1.6
		RMSD bond lengths (Å)	0.003
Distance restraints		RMSD bond angles (°)	0.4
Total distance restraints	1760		
Intra-residue ($\|i-j\|=0$)	420	Molprobity Ramachandran statistics[a,b]	
Sequential ($\|i-j\|=1$)	487	Most favored regions (%)	98.1
Medium range ($\|i-j\|>1$ and $\|i-j\|<5$)	262	Allowed regions (%)	1.9
Long range ($\|i-j\|\geq 5$)	591	Disallowed regions (%)	0
No. of restraints per residue	14.5		
No. of long-range restraints per residue	4.9	Global quality scores (raw/Z score)[a,b]	
		Verify3D	0.27/−3.05
Distance restraint violations per model		ProsaII	0.85/0.83
0.1–0.2 (Small)	0.1	Procheck (phi-psi)	−0.06/0.08
0.2–0.5 (Medium)	None	Procheck (all)	−0.14/−0.83
>0.5 (Large)	None	Molprobity clashscore	7.33/0.27
Model content		Identifiers	
Ordered residue ranges	8–118	PDB ID	9QUX
Total no. of residues	121	BMRB ID	34990

Note: If not indicated otherwise, data are from the standard PDB validation report.
[a]Calculated using PSVS.
[b]Calculated for ordered residues (8-118).

40–43. The former, longer loop forms the tip of a beta-hairpin that contributes a number of residues to the partner binding site (Figure 2C). In the majority of Homer1 EVH1 crystal structures, the conformation of this loop is highly similar, regardless of whether they are in the free or in a bound state (Figures 2C, S6, and Table S2). According to analysis with ePISA [43], this loop participates in crystal contacts with neighboring molecules, providing a possible explanation for this observation. The only Homer1 x-ray structure with a different loop conformation is 1i2h, which represents an EVH1 domain binding to the P-motif (SPLTP) of neighboring Homer1 molecules in the crystal [3]. Considering other available EVH1 domain structures, this region shows yet again different conformations in Enabled, N-WASP and Spred2 proteins; thus, we speculate that this loop might undergo minor rearrangements upon partner binding. This hypothesis is further supported by the comparison of the N-WASP EVH1 NMR structures available under PDB IDs 1mke and 2ifs representing complexes with different ligands (as fusion constructs), where these loops also adopt different conformations (Figure S7). In addition, in our NMR ensemble the indole ring of Trp24 displays an orientation that is almost perpendicular to those observed in the other EVH1 structures (Figure 2D). Trp24 is one of the key residues involved in partner binding, and the reorientation of its side chain might well accompany the binding of the partner Pro-rich sequences as the aromatic cluster of Phe14, Trp24 and Phe74 reorganizes to accommodate the pyrrolidine rings.

3.3 | Backbone Dynamics of the EVH1 Domain

The rotational correlation time estimated from the T_1/T_2 ratio with Tensor2 is 7.89 ns. Residues with excluded hetNOE values reside in the termini with the sole exception of Asn23, having a hetNOE value slightly above 1.0. The obtained S^2 order parameters are generally over 0.85 with only 4 values below 0.8, indicating a stable globular structure. The lowest S^2 values are in the segments 13–15 and 83–86, two neighboring β-strands around the ligand-binding site, as well as residues 102–105 in the C-terminal helix (Figure 3A). Residues with substantial (> 2.5 1/s) R_{ex} contribution are largely clustered in and near the N-terminal region of the helix. Notable other residues affected are Val28, located near the ligand-binding site, as well as residues Asp39 and Val44 forming H-bonds with each other at the turn between strands 2 and 3 (Figures 3B and S8). These residues are located near sites where conformational differences

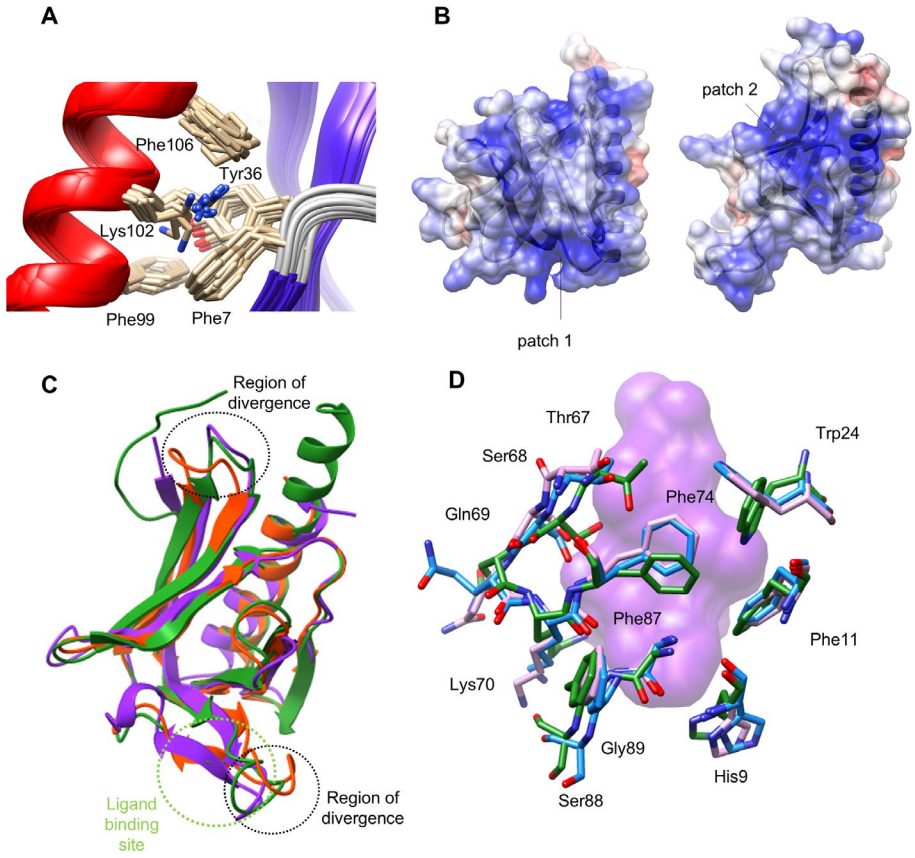

FIGURE 2 | Local features of the EVH1 structure. (A) The putative cation-pi interaction between Lys102, Phe7, Tyr36, Phe99 and Phe106 in the NMR ensemble. (B) Electrostatic surface of the Homer1 EVH1, illustrated using the medoid model in the ensemble. Blue shades depict positive, red shades negative surface areas. (C) comparison of EVH1 domains. Green: The NMR ensemble described in the present study. Regions of divergence between the other structure and our structure is marked (black) and the ligand binding site is also indicated (light green). Orange red: Other available Homer1 EVH1 structure (PDB ID: 1ddv). Purple: Additional EVH1 structure (PDB ID: 1evh). (D) Orientation of the ligand-binding residues in the medoid structure of our NMR ensemble (color by atom type), the structure 1ddw (without ligand, blue) and 1ddv (liganded, purple). The position of the ligand in the entry 1ddv (mGluR peptide) is shown with a semi-transparent purple surface. Note that we use residue numbers corresponding to the UniProt sequence (Q9Z2Y3), whereas the PDB entry contains a 3-residue expression tag and is numbered accordingly.

between the unliganded solution NMR structure and the x-ray structures (e.g., PDB ID: 1ddv) are observed, again reinforcing the possibility of subtle structural rearrangements upon ligand binding. In this respect, we also note that, when included, residue Thr70, also near the ligand-binding site, shows a large R_{ex} contribution, but in the final analysis this residue was omitted because of severe signal overlap with the amide peak of Ser35 (Figures 3C, S8, Table S3).

Comparing our results to the available solution dynamics of the distantly related dynamin1 PH domain [44], it is apparent that in the PH domain the distribution of residues with substantial R_{ex} contribution is quite different from that in the Homer1 EVH1 domain, with the patch in the helix missing entirely. However, residues Asp79, Thr84, and Tyr86, located near the turn linking β-strands 6 and 7 are in a similar position to a cluster of residues with high R_{ex} values in the dynamin1 PH domain (depicted on the x-ray structure with the PDB ID 1dyn) [45]. These results might indicate the presence of both conserved and unique dynamical features in the large domain family (Figures 3C, S8, Table S3).

3.4 | Modeling the Coiled Coil Region

To model the full-length Homer1 (Homer1c isoform), we used the available experimentally solved structures of the globular EVH1 domain (PDB ID: 1ddv [24]) and the C-terminal fragment forming a four-stranded antiparallel coiled coil (PDB ID: 3cve [6]) (Figure S9). Since both the N- and C-terminal regions are only determined for the *Rattus norvegicus* protein, we chose to model the full-length Homer1 of this species. The sequential differences between rat, mouse and human are shown in Figure S2. Generally, the EVH1 domain is extremely conserved and the coiled coil segment only contains a handful of substitutions, while the major difference between the species is detectable in the length of the disordered region. For the modeling, we used an approach to connect the existing experimental structures with the modeling of the middle segment of the protein, which represented a disordered region and a dimeric coiled coil. Firstly, the characteristic parameters (radius, pitch, interface angle) of the tetramer structure were determined. Based on these characteristics, the long coiled coil regions were modeled first with CCbuilder [26]

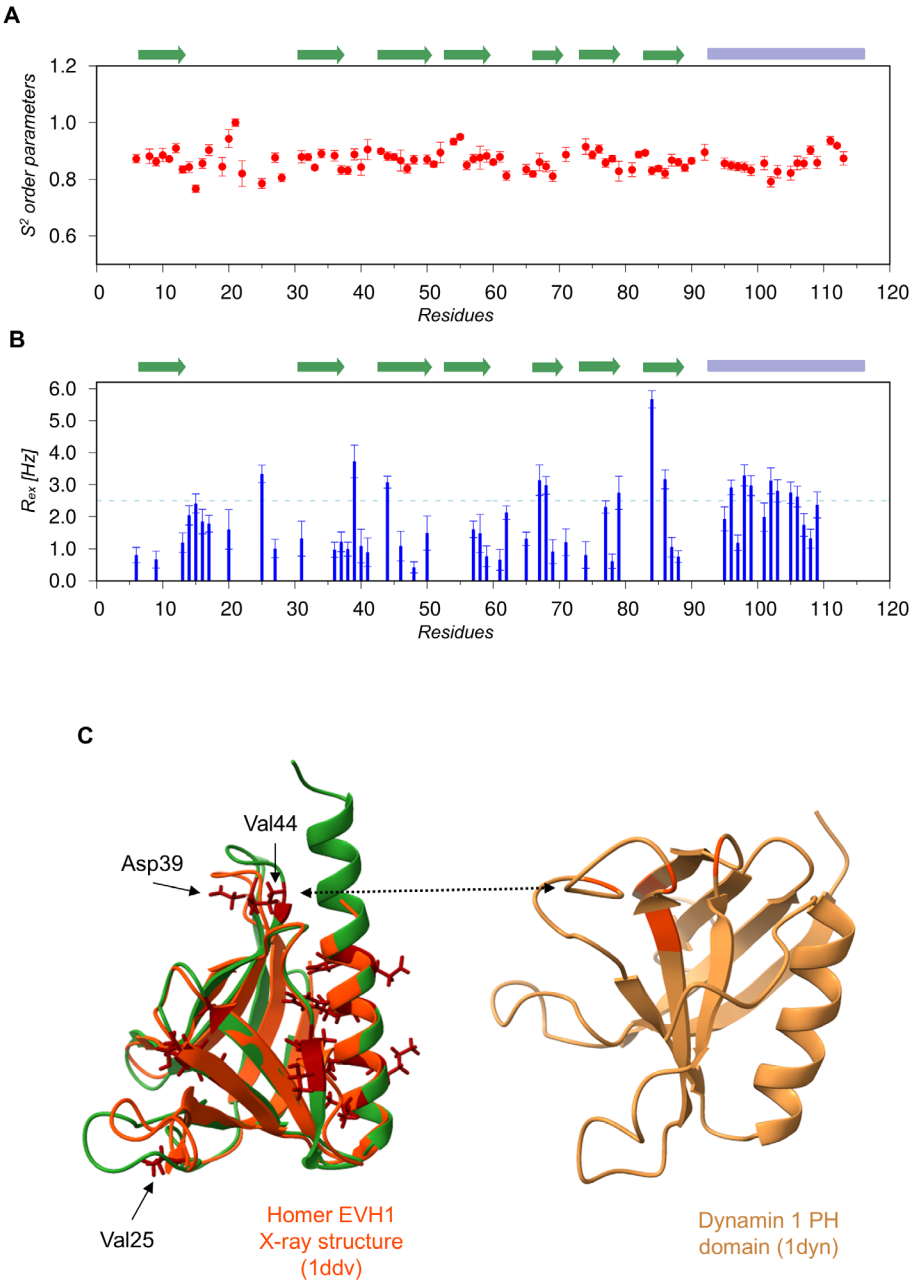

FIGURE 3 | The dynamics of the EVH1 domain. (A) S2 order parameters calculated for the domain. (B) R_{ex} contribution of residues as obtained from the Model-free analysis. (C) Residues with substantial R_{ex} contribution in the Homer1 EVH1 domain are marked with red. Besides those located in the N-terminal region of the helix, Val25, Asp39 and Val44 (residue numbers corresponding to UniProt entry Q9Z2Y3) are in regions where there are characteristic conformational differences relative to available x-ray structures, (green: Our model, orange: PDB entry 1ddv). There are also affected residues located in a region corresponding to a cluster of residues with high R_{ex} values in the dynamin PH domain (beige: PDB entry 1 dyn).

and later with Isambard [27], exploring different settings. The parallel long chains were aligned to the tetramer and inspected visually. Only residues 112–189, linking the EVH1 domain to the coiled coil region, were modeled explicitly as disordered (see Methods). It is expected that there are other fully or partially disordered regions within the dimeric coiled coil region or at the transitional structure between the two- and four-stranded coiled coil segments. However, we decided against including any such intermediate disordered regions in the initial model as their boundaries could not be precisely predicted. The challenges of modeling a long coiled coil with alternating regular and unfolded segments include proper linking of the different regions while maintaining regularity in the superhelical segments, which could introduce unrealistic structural features that could be hard to correct at later stages. Our working hypothesis was that flexible regions modeled as coiled coils will turn out to be unstable during the molecular dynamics simulations, providing a better estimate of the actual dynamics of the region than those deducible from sequence-based predictions only.

3.5 | Molecular Dynamics Simulation of the Dimeric and Tetrameric Form of Full-Length Homer1

Multiple rounds of all-atom molecular dynamics simulations in explicit water were carried out for both the dimer form and the tetramer (more than 11 000 atoms) for 200 ns per run. For the dimeric structure, five parallel runs with different random initial velocities were used and will be referred to as dimer_1–dimer_5. The simulated trajectories were converted to 20 000 models/run for the dimer and 1000 models for the tetramer. The parallel runs capture quite different dynamics and conformations of the models, that is supported by the trends of the calculated all-atom RMSDs during the simulations (Figure S10).

Our main findings relate to the dimeric form, as we have several parallel longer runs available for this case. Analysis of the secondary structure and the formation of knobs-into-holes interactions, characteristic of coiled coils were performed using DSSP [32] and SOCKET [29], respectively. This analysis showed that the stability of the superhelical structure, as expected, is not uniform along the modeled coiled coil (Figure 4). It is important to note that there are several substantial differences observed between the simulation trajectories; therefore, we will focus on the commonly occurring features unless noted otherwise. Considering the consensus of the five MD runs, two stable regions can be identified, one covering residues 260–270 and the other spanning residues 300–325. In one of the simulations (dimer_1), the whole C-terminal segment of the coiled coil from residue 250 remains stable (Table S4). This observation seems to be largely independent of the initial conformation, as we run a shorter simulation on an AlphaFold predicted dimer (Figure S11) and these regions showed similar tendencies regarding flexibility. The distribution of intermolecular salt bridges fits well with the stability data if we consider heptad positions. There are five possible pairs formed between residues in heptad position "e" in one chain and "g" in the other. These pairs are located in positions 258–260, 302–307, 309–314, and 321–323 and they can be consistently identified in each simulation (Figure 4). Outside of this region (residues 190–250), we did not observe any straightforward relationships between coiled coil stability, assigned heptad positions and possible salt bridges, indicating a more complex dynamic behavior of the N-terminal part of the long coiled coil. Interestingly, intramolecular salt bridge formation shows substantial variability in the different runs, especially in the N-terminal region of the coiled coil (residue 190–270). The region 270–295 exhibits different interaction patterns in the individual runs, but only maintains the coiled coil conformation during the dimer_1 simulation.

Analysis of Cα-Cα distances between identical residues in the interacting chains forming the coiled coil offers another means to assess the flexibility of the structure. These distances exhibit a periodicity according to the positions in the heptad repeats, but also show variability for residues in the same positions but in different regions, indicating non-uniform stability along the superhelical structure. The observed enlarged Cα-Cα distances are consistent with the results of the DSSP [32] and SOCKET [29] analysis and also indicate partial local unfolding of the coiled coil (Figure 4). There is an extremely regular segment of the coiled coil aligning with the second stable region (residue 300–325) where Cα-Cα distances are extremely similar for each run and consistent with the buried nature of residues in positions "a" and "d." This segment also shows a highly regular pattern of buried and exposed residues—in accordance with their position in the heptad (Figure 4). We investigated whether the structurally more stable segments show higher evolutionary conservation at the sequence level. Shannon-entropy calculated for the individual residue positions shows surprisingly high conservation at the N-terminal region of the coiled coil that proved to be the most unstable during our simulations (Figure 4).

The dimeric Homer1 models exhibit high structural flexibility, resulting in different kinds of structural rearrangements leading to different global shapes of the assembly and different relative positions and orientations of the EVH1 domains (Figure 5). We have analyzed three aspects of such structural features: (a) the distance between the two EVH1 domains (b) the presence of kinks within the coiled coil (c) the rotation of the two binding pockets in the EVH1 domains relative to each other. The distance between the two EVH1 domains, measured between the positions calculated from the average of the domains, can vary substantially from a maximum of over 200 Å to a minimum distance of 40 Å (Figure S12A). This distance decreases with time during our molecular dynamics simulations. This certainly does not adequately describe the cellular behavior of the system, but it highlights the large distances that even such a dimeric complex can bridge, and also shows (in the case of dimer_3 and dimer_5, most notably in the 0–100 ns time scale) how dynamically this distance can evolve (Figure S12B). The rotation of EVH1 domains with respect to each other is highly heterogeneous for different models. The long disordered region provides a very high degree of flexibility in the spatial location of the domains, which can be important for binding to different partners (Figure S12C). The motion resulting from the kinking of the coiled coil reflects its structural flexibility in the dimeric state in comparison to the tetramer that seems to be more rigid in this manner (Figure S12D).

Based on an interaction observed in the crystalline state, Homer1 EVH1 was previously suggested to bind to its internal P-motif, although this could not be confirmed in solution [3]. Nevertheless, the presence of such an interaction cannot be readily dismissed in a crowded environment and, especially, in the context of a multimeric protein. Therefore, we have investigated whether this interaction could occur in the context of the tetrameric form either within a single Homer1 chain or between neighboring chains in the complex. From our initial modeling it seems that the formation of an intrachain interaction between the P-motif and the EVH1 domain is sterically possible, however the small helical fragment at the C-terminal of the EVH1 domain should not be longer than 15 residues (Figure S13). There are also variations in the length of the helix in the available crystal structures.

4 | Discussion

In this study, we have explored the structure of the full-length Homer1 protein, using NMR spectroscopy to provide the first solution structure of the globular EVH1 domain and applying modeling and molecular dynamics for the characterization

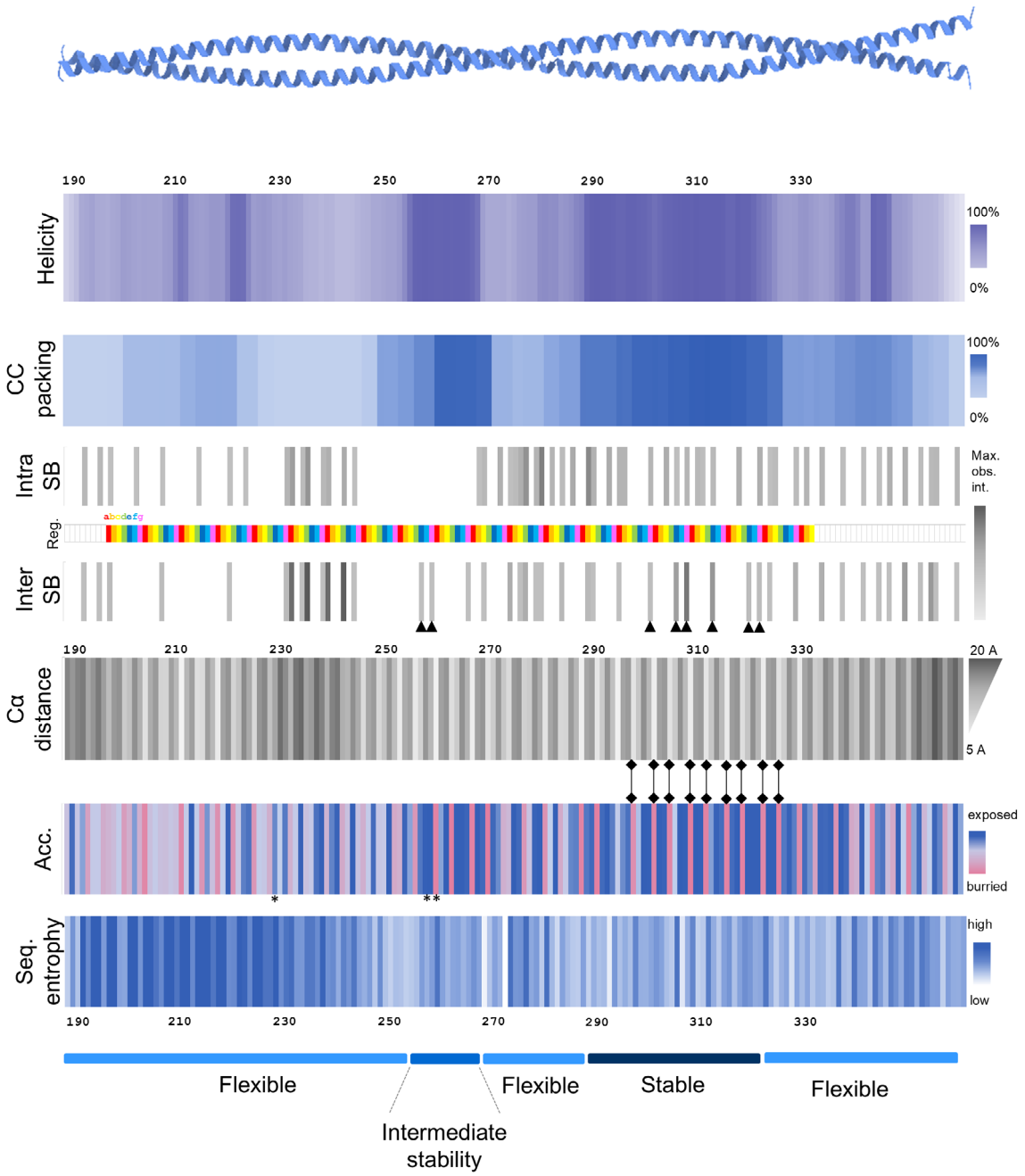

FIGURE 4 | Analysis of coiled coil stability in the dimeric model. Different panels show the aspects of the observed differences in the structural stability along the coiled coil. The average of the five parallel runs was calculated and plotted. Panels: (A) Predicted stable helical segments during the simulations are in shade of dark purple (DSSP [32]). (B) Predicted stable coiled coil segments during the simulations are in shade of dark blue (SOCKET [29]). (C) Possible intrachain salt bridge formation, the darker gray shows more detected interactions, (D) Heptad positions along the coiled coil (Coloring according SOCKET-defined heptad positions: "a"-red, "b"-orange, "c"-yellow, "d"-green, "e"-dark blue, "f"-light blue, "g"-pink), (E) Possible interchain salt bridge formation; arrows indicating "e" and "g" positions in the heptad repeat (F) Average Cα distances between the two coiled coil chains, (G) Average accessibility of the position during simulation. For the C-terminal segment, several amino acids in position 'a' and 'd' show regular patterns in (F) and (G). (H) Shannon entropy in vertebrates: The more conserved positions are the darker. (I) Five distinguishable regions of the coiled coil segment (Numerical data is available in Table S4).

of the coiled coil region. The solution structure of the EVH1 domain aligns well with the overall fold of previously determined EVH1 structures, but also suggests the presence of subtle structural rearrangements upon ligand binding. The local conformation around the ligand-binding region, especially residues 18–21, forming a turn after the first beta strand, is different from that observed in the available Homer EVH1 x-ray structures. On the other hand, this region exhibits variability when considering a larger set of EVH1 domains, lending support to the hypothesis that this segment can undergo functionally relevant motions. This is supported by the observed solution-state dynamics of the EVH1 domain where residues with substantial R_{ex} contribution are located near loops that exhibit differences relative to the previously determined

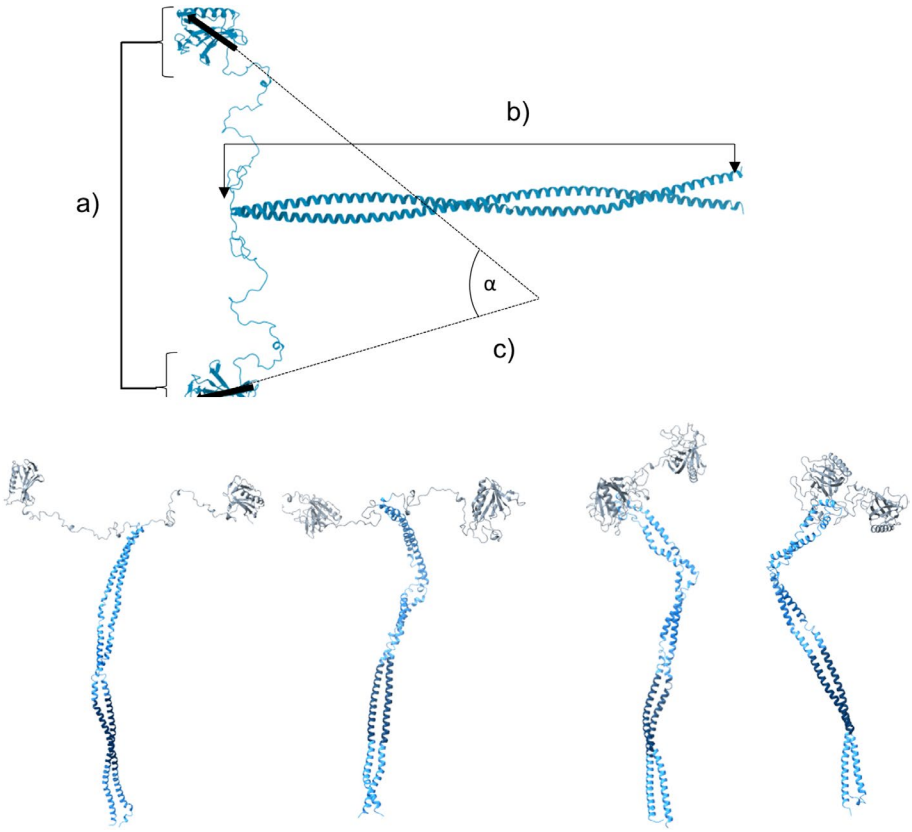

FIGURE 5 | The analyzed features of the flexibility shown of the structure (A) distance of the average position in the domain, (B) distance of the N and C-terminal of the coiled coil and (C) rotation of the two binding pockets in the EVH1 domains relative to each other in 3D. Structures representing the structural flexibility of the dimeric Homer1. Coloring according to the five regions with different stability as depicted in Figure 4 panel I.

x-ray structures. The possible functional relevance of such rearrangements, as well as of the positively charged surface patches, especially that of patch 2, located relatively far from the described ligand binding site, remains to be explored. The cluster of residues with R_{ex} contribution in the C-terminal helix might be speculated to indicate the presence of weak intermolecular interactions; however, this seems unlikely based on our SAXS data, producing an excellent fit to the monomeric structure. Further studies, including the detailed mapping of the slow timescale dynamics of the domain might be needed to clarify this aspect.

To explore the architecture of the full Homer1 tetramer, we first characterized the long dimeric coiled coil region of the molecule. For this, we have applied a complex pipeline using tools specifically designed for coiled coil modeling and analysis. Although we considered using general-purpose tools like AlphaFold-Multimer [34], we decided to perform the task with computational tools specifically developed for coiled coil modeling. This pipeline provided an explainable and configurable framework and is also expected to properly take into account the characteristic overall geometry and side chain packing features of coiled coils. To build an architectural model of the tetrameric assembly, we have used the available x-ray structure of the tetramerization region and fitted a model of the long dimeric coiled coil to it. The resulting models, containing either a dimeric segment or the full tetrameric assembly, were analyzed to assess their dynamics and stability features. Our molecular dynamics simulations indicate the presence of segments with different stability and flexibility in the long coiled coil region, with the most stable region being the C-terminal segment next to the tetramerization domain. The increased flexibility towards the N-terminal part of the coiled coil makes it possible for the full tetramer to adopt various global shapes besides the fully extended linear one. This kind of flexibility in long coiled coil segments has been observed for other proteins both with experimental and theoretical methods. The intramolecular coiled coil of Rad50 also showed irregular flexibility in its long coiled coil segment [46]. Tropomyosin coiled coil flexibility is also required for its function [47]. The kink formation was revealed for laminin supported by experimental data measured with atomic force microscopy and also observed in coarse-grained MD simulations [48].

The residue conservation pattern of Homer1 segments does not correspond to the location of stable and unstable coiled coil segments identified by our simulations. However, it must be noted that conservation indicates functional importance and not necessarily structural stability. Thus, it can be speculated that the observed conservation features indicate that a precisely tuned flexibility is necessary to maintain Homer1 function. Moreover, the higher flexibility of this region relative to the C-terminal part does not exclude its role in initiating multimerization, as is currently proposed for cotranslational assembly of protein complexes [49], and is well in line with our earlier observations on the importance of such regions based on the pattern of germline mutations [50].

The presence of kinked structures within the coiled coil and the flexibility of the disordered linker enable a wide range of relative distances and orientations for the four EVH1 domains in the tetramer. Thus, the full-length Homer might not only bridge large distances, but could also provide a permanent physical link between partner molecules and complexes during larger structural rearrangements within the postsynaptic protein network. It should be noted that for our full model we have used the already available x-ray structure instead of the NMR ensemble determined in this work. However, this choice does not affect the overall architecture or flexibility of the full tetramer. The possible structural rearrangements upon ligand binding in the EVH1 domain might, in principle, propagate to the linker region or even further, but we do not expect that such events can be accurately modeled with the molecular dynamics calculations performed here and would need experimental verification, which, given the complexity of the full tetramer, is an especially challenging task.

The role Homer fulfills in synapse might be essential; the EVH1 domain is highly conserved, Even the Drosophila sequence has remarkable identity to the human protein. The coiled coil segment has also changed relatively little in vertebrates. It might also be speculated that the EVH1 domain might not be the only region that can participate in various protein:protein interactions, and these additional interactions might play a role in modulating the flexibility of the coiled coil rod. The best candidate for such an interaction is the P-motif, capable of forming complexes with the EVH1 domain in the crystalline state, although not in solution [3]. Still, its conservation within a disordered segment is best explained by its role as a potential binding motif, and it might also be possible that the same applies to the conserved yet flexible N-terminal part of the long coiled coil. Our results altogether suggest that Homer1 does not only act as a passive linker between its partners but might have more complex roles in the organization of the postsynaptic protein network.

Author Contributions

Zsófia E. Kálmán: investigation, visualization, writing – original draft, formal analysis. **András Czajlik:** investigation, formal analysis. **Brigitta Maruzs:** investigation, formal analysis. **Fanni Farkas:** investigation, writing – original draft, formal analysis. **István Pap:** investigation. **Csilla Homonnay:** investigation. **Tomas Klumpler:** investigation, writing – original draft. **Gyula Batta:** investigation, conceptualization. **Zoltán Gáspári:** investigation, conceptualization, writing – original draft, visualization, supervision, funding acquisition. **Bálint Péterfia:** investigation, conceptualization, writing – review and editing, supervision.

Acknowledgments

This work was supported by the Hungarian National Research, Development and Innovation Office (NKFIH) (grants, OTKA K 137947, TKP2021-EGA-42, and 2021-4.1.2-NEMZ_KI-2022-00027). We acknowledge Digital Government Development and Project Management Ltd. for awarding us access to the Komondor HPC facility based in Hungary. The research (G.B.) was supported by the University of Debrecen, Scientific Research Bridging Fund (DETKA) and by the EU and cofinanced by the European Regional Development Fund under the projects GINOP-2.3.2-15-2016-00008 (G.B.) and GINOP-2.3.3-15-2016-00004 (access to Bruker NEO 700 MHz NMR spectrometer). The authors are grateful to Gitta Schlosser for the HPLC-MS measurements, and to Viktor Farkas for the supervision of CD spectroscopy measurements. We acknowledge CF Biomolecular Interactions and Crystallography of CIISB, Instruct-CZ Centre, supported by MEYS CR (LM2023042) and European Regional Development Fund–Project "Innovation of Czech Infrastructure for Integrative Structural Biology" (No. CZ.02.01.01/00/23_015/0008175).

Data Availability Statement

Nuclear magnetic resonance data for the structural ensemble reported in this article have been deposited at the Biological Magnetic Resonance Data Bank, under deposition ID:34990. The NMR structure of the EVH1 domain is deposited in PDB and accessible under the ID:9QUX. The corresponding small-angle X-ray scattering data have been deposited in the Small Angle Scattering Biological Data Bank with the ID: SASDXK2. The modeled Homer1 tetramer is available in ModellArchive with the following ID: ma-cp0vl.

Peer Review

The peer review history for this article is available at https://www.webofscience.com/api/gateway/wos/peer-review/10.1002/prot.70091.

References

1. W. J. Droogers and H. D. MacGillavry, "Plasticity of Postsynaptic Nanostructure," *Molecular and Cellular Neuroscience* 124 (2023): 103819.

2. A. de Bartolomeis and G. Fiore, "Postsynaptic Density Scaffolding Proteins at Excitatory Synapse and Disorders of Synaptic Plasticity: Implications for Human Behavior Pathologies," *International Review of Neurobiology* 59 (2004): 221–254.

3. K. Irie, T. Nakatsu, K. Mitsuoka, et al., "Crystal Structure of the Homer 1 Family Conserved Region Reveals the Interaction Between the EVH1 Domain and Own Proline-Rich Motif," *Journal of Molecular Biology* 318, no. 4 (2002): 1117–1126.

4. Y. Shiraishi-Yamaguchi and T. Furuichi, "The Homer Family Proteins," *Genome Biology* 8 (2007): 1–12.

5. M. K. Hayashi, H. M. Ames, and Y. Hayashi, "Tetrameric Hub Structure of Postsynaptic Scaffolding Protein Homer," *Journal of Neuroscience* 26, no. 33 (2006): 8492–8501.

6. M. Hayashi, C. Tang, C. Verpelli, et al., "The Postsynaptic Density Proteins Homer and Shank Form a Polymeric Network Structure," *Neuroscience Research* 68 (2010): e339.

7. L. J. Ball, T. Jarchau, H. Oschkinat, and U. Walter, "EVH1 Domains: Structure, Function and Interactions," *FEBS Letters* 513, no. 1 (2002): 45–52.

8. A. de Bartolomeis, A. Barone, E. F. Buonaguro, C. Tomasetti, L. Vellucci, and F. Iasevoli, "The Homer1 Family of Proteins at the Crossroad of Dopamine-Glutamate Signaling: An Emerging Molecular "Lego" in the Pathophysiology of Psychiatric Disorders. A Systematic Review and Translational Insight," *Neuroscience & Biobehavioral Reviews* 136 (2022): 104596.

9. G. H. Diering, R. S. Nirujogi, R. H. Roth, P. F. Worley, A. Pandey, and R. L. Huganir, "Homer1a Drives Homeostatic Scaling-Down of Excitatory Synapses During Sleep," *Science* 355, no. 6324 (2017): 511–515.

10. J. P. Yuan, K. Kiselyov, D. M. Shin, et al., "Homer Binds TRPC Family Channels and Is Required for Gating of TRPC1 by IP3 Receptors," *Cell* 114, no. 6 (2003): 777–789.

11. J. Marley, M. Lu, and C. Bracken, "A Method for Efficient Isotopic Labeling of Recombinant Proteins," *Journal of Biomolecular NMR* 20 (2001): 71–75.

12. F. W. Studier, "Stable Expression Clones and Auto-Induction for Protein Production in *E. coli*," in *Structural Genomics: General Applications* (Humana Press, 2013), 17–32.

13. A. Micsonai, É. Moussong, F. Wien, et al., "BeStSel: Webserver for Secondary Structure and Fold Prediction for Protein CD Spectroscopy," *Nucleic Acids Research* 50, no. W1 (2022): W90–W98.

14. P. Güntert, "Automated NMR Structure Calculation With CYANA," *Protein NMR Techniques* 278 (2004): 353–378.

15. Y. Shen and A. Bax, "Protein Structural Information Derived From NMR Chemical Shift With the Neural Network Program TALOS-N," *Artificial Neural Networks* 1260 (2015): 17–32.

16. G. A. Bermejo, N. Tjandra, G. M. Clore, and C. D. Schwieters, "XplorNIH: Better Parameters and Protocols for NMR Protein Structure Determination," *Protein Science* 33, no. 4 (2024): e4922.

17. A. Bhattacharya, R. Tejero, and G. T. Montelione, "Evaluating Protein Structures Determined by Structural Genomics Consortia," *Proteins: Structure, Function, and Bioinformatics* 66, no. 4 (2007): 778–795.

18. R. Koradi, M. Billeter, and K. Wüthrich, "MOLMOL: A Program for Display and Analysis of Macromolecular Structures," *Journal of Molecular Graphics* 14, no. 1 (1996): 51–55.

19. E. F. Pettersen, T. D. Goddard, C. C. Huang, et al., "UCSF Chimera—A Visualization System for Exploratory Research and Analysis," *Journal of Computational Chemistry* 25, no. 13 (2004): 1605–1612.

20. E. Jurrus, D. Engel, K. Star, et al., "Improvements to the APBS Biomolecular Solvation Software Suite," *Protein Science* 27, no. 1 (2018): 112–128.

21. W. Lee, M. Tonelli, and J. L. Markley, "NMRFAM-SPARKY: Enhanced Software for Biomolecular NMR Spectroscopy," *Bioinformatics* 31, no. 8 (2015): 1325–1327.

22. P. Dosset, J. C. Hus, M. Blackledge, and D. Marion, "Efficient Analysis of Macromolecular Rotational Diffusion From Heteronuclear Relaxation Data," *Journal of Biomolecular NMR* 16, no. 1 (2000): 23–28.

23. S. Grudinin, M. Garkavenko, and A. Kazennov, "Pepsi-SAXS: An Adaptive Method for Rapid and Accurate Computation of Small-Angle X-Ray Scattering Profiles," *Acta Crystallographica Section D, Structural Biology* 73, no. 5 (2017): 449–464.

24. J. Beneken, J. C. Tu, B. Xiao, et al., "Structure of the Homer EVH1 Domain-Peptide Complex Reveals a New Twist in Polyproline Recognition," *Neuron* 26, no. 1 (2000): 143–154.

25. D. Piovesan, A. del Conte, D. Clementel, et al., "MobiDB: 10 Years of Intrinsically Disordered Proteins," *Nucleic Acids Research* 51, no. D1 (2023): D438–D444.

26. C. W. Wood and D. N. Woolfson, "C CB Uilder 2.0: Powerful and Accessible Coiled-Coil Modeling," *Protein Science* 27, no. 1 (2018): 103–111.

27. C. W. Wood, J. W. Heal, A. R. Thomson, et al., "ISAMBARD: An Open-Source Computational Environment for Biomolecular Analysis, Modelling and Design," *Bioinformatics* 33, no. 19 (2017): 3043–3050.

28. Z. Harmat, D. Dudola, and Z. Gáspári, "DIPEND: An Open-Source Pipeline to Generate Ensembles of Disordered Segments Using Neighbor-Dependent Backbone Preferences," *Biomolecules* 11, no. 10 (2021): 1505.

29. J. Walshaw and D. N. Woolfson, "Socket: A Program for Identifying and Analysing Coiled-Coil Motifs Within Protein Structures," *Journal of Molecular Biology* 307, no. 5 (2001): 1427–1450.

30. J. Delgado, L. G. Radusky, D. Cianferoni, and L. Serrano, "FoldX 5.0: Working With RNA, Small Molecules and a New Graphical Interface," *Bioinformatics* 35, no. 20 (2019): 4168–4169.

31. D. van der Spoel, E. Lindahl, B. Hess, G. Groenhof, A. E. Mark, and H. J. Berendsen, "GROMACS: Fast, Flexible, and Free," *Journal of Computational Chemistry* 26, no. 16 (2005): 1701–1718.

32. W. Kabsch and C. Sander, "Dictionary of Protein Secondary Structure: Pattern Recognition of Hydrogen-Bonded and Geometrical Features," *Biopolymers* 22, no. 12 (1983): 2577–2637.

33. M. Mirdita, K. Schütze, Y. Moriwaki, L. Heo, S. Ovchinnikov, and M. Steinegger, "ColabFold: Making Protein Folding Accessible to all," *Nature Methods* 19, no. 6 (2022): 679–682.

34. J. Abramson, J. Adler, J. Dunger, et al., "Accurate Structure Prediction of Biomolecular Interactions With AlphaFold 3," *Nature* 630, no. 8016 (2024): 493–500.

35. J. B. Procter, G. M. Carstairs, B. Soares, et al., "Alignment of Biological Sequences With Jalview," in *Methods in Molecular Biology* (Springer US, 2021), 203–224.

36. A. M. Altenhoff, C. M. Train, K. J. Gilbert, et al., "OMA Orthology in 2021: Website Overhaul, Conserved Isoforms, Ancestral Gene Order and More," *Nucleic Acids Research* 49, no. D1 (2021): D373–D379.

37. M. Saraste and M. Hyvönen, "Pleckstrin Homology Domains: A Fact File," *Current Opinion in Structural Biology* 5, no. 3 (1995): 403–408.

38. P. N. Cheng, J. D. Pham, and J. S. Nowick, "The Supramolecular Chemistry of β-Sheets," *Journal of the American Chemical Society* 135, no. 15 (2013): 5477–5492.

39. C. A. Andersen, A. G. Palmer, S. Brunak, and B. Rost, "Continuum Secondary Structure Captures Protein Flexibility," *Structure* 10, no. 2 (2002): 175–184.

40. M. Barzik, U. D. Carl, W. D. Schubert, R. Frank, J. Wehland, and D. W. Heinz, "The N-Terminal Domain of Homer/Vesl Is a New Class II EVH1 Domain," *Journal of Molecular Biology* 309, no. 1 (2001): 155–169.

41. G. N. Huang, D. L. Huso, S. Bouyain, et al., "NFAT Binding and Regulation of T Cell Activation by the Cytoplasmic Scaffolding Homer Proteins," *Science* 319, no. 5862 (2008): 476–481.

42. Z. Li, H. Liu, J. Li, et al., "Homer Tetramer Promotes Actin Bundling Activity of Drebrin," *Structure* 27, no. 1 (2019): 27–38.

43. E. Krissinel, "Protein Interfaces, Surfaces and Assemblies Service PISA at European Bioinformatics Institute," *Journal of Molecular Biology* 372 (2007): 774.

44. D. Fushman, S. Cahill, and D. Cowburn, "The Main-Chain Dynamics of the Dynamin Pleckstrin Homology (PH) Domain in Solution: Analysis of 15N Relaxation With Monomer/Dimer Equilibration," *Journal of Molecular Biology* 266, no. 1 (1997): 173–194.

45. K. M. Ferguson, M. A. Lemmon, J. Schlessinger, and P. B. Sigler, "Crystal Structure at 2.2 Å Resolution of the Pleckstrin Homology Domain From Human Dynamin," *Cell* 79, no. 2 (1994): 199–209.

46. J. van Noort, T. van Der Heijden, M. de Jager, C. Wyman, R. Kanaar, and C. Dekker, "The Coiled-Coil of the Human Rad50 DNA Repair Protein Contains Specific Segments of Increased Flexibility," *Proceedings of the National Academy of Sciences* 100, no. 13 (2003): 7581–7586.

47. A. Singh and S. E. Hitchcock-DeGregori, "Dual Requirement for Flexibility and Specificity for Binding of the Coiled-Coil Tropomyosin to Its Target, Actin," *Structure* 14, no. 1 (2006): 43–50.

48. L. Akter, H. Flechsig, A. Marchesi, and C. M. Franz, "Observing Dynamic Conformational Changes Within the Coiled-Coil Domain of Different Laminin Isoforms Using High-Speed Atomic Force Microscopy," *International Journal of Molecular Sciences* 25, no. 4 (2024): 1951.

49. M. Badonyi and J. A. Marsh, "Hallmarks and Evolutionary Drivers of Cotranslational Protein Complex Assembly," *FEBS Journal* 291, no. 16 (2024): 3557–3567.

50. Z. E. Kalman, B. Mészáros, Z. Gáspári, and L. Dobson, "Distribution of Disease-Causing Germline Mutations in Coiled-Coils Implies an Important Role of Their N-Terminal Region," *Scientific Reports* 10, no. 1 (2020): 17333.

Supporting Information

Additional supporting information can be found online in the Supporting Information section. **Data S1:** prot70091-sup-0001-Tables.

xlsx. **Figure S1:** Top: Isoforms of murine Homer1 proteins. Bottom: Schematic figure on the tetramerization of Homer1c. Experimental structures are only available for the EVH1 domain (see Table S2) and the tetrameric coiled coil region (PDB: 3CVE) [4, 5]. **Figure S2:** Multiple sequence alignment of the Human (Q86YM7), Mouse (Q9Z2Y3) and Rat (Q9Z214) Homer1 sequences. Conservation (yellow top), quality (yellow bottom) scores and the consensus sequence (black), along with structural annotation are depicted below the alignment. The canonical isoforms available in UniProt as of February 2025 were used. Alignment and visualization were performed using Jalview. **Figure S3:** SDS-PAGE showing the purification steps of the EVH1 domain. The TEV-cleaved form migrates at 13 kDa as expected. **Figure S4:** ^{1}H-^{15}N HSQC spectrum of EVH1 exhibits signal dispersion characteristic of globular protein. Peak labels show the assigned residues. **Figure S5:** Stereo view of the structures calculated for the EVH1 domain. **Figure S6:** Structural comparison of the EVH1 domains. Green: the NMR ensemble described in the present study. Orange: other available Homer1 EVH1 structures. Purple: additional EVH1 structures, listed in Table S3. To help visual comparison, additional chains were removed and some structures were truncated at their C-terminus. (extended version of Figure 2C). **Figure S7:** Structure comparison of EVH1 NMR structures reveals variability in the loop regions near the binding site. Brown: 1mke (N-WASP EVH1 in complex with a fused WIP protein segment, only the EVH1 domain is shown), blue: 2ifs (N-WASP EVH1 domain in complex with a fused WIP protein segment, only the EVH1 domain is shown), green: 2jp2 (EVH1 domain of the human Spred2 protein), magenta: Homer1 EVH1 domain determined in this study. **Figure S8:** Fitted Relaxation data for the Homer1 EVH1 domain. A and B: R_1 and R_2 relaxation rates, respectively. The smoothed Bezier curves are shown only to guide the eye. All fitted values are shown. C: T_1/T_2 ratio for the residues. Data obtained from peaks with substantial overlap are shown in light green. The horizontal lines show the average ±1 standard deviation of the T_1/T_2 rates calculated from the non-overlapping peaks. Data outside this range were not used for the estimation of the diffusion tensor. D: heteronulcear ^{15}N NOE values for all residues. Values not used in the model-free calculation are shown in magenta. The large negative value for residue 117 is shown beside the respective bar. **Figure S9:** Modeling of the tetramer coiled-coil. MobiDB was used to determine the boundary between the coiled-coil and the disordered segment. The PDB ids 1ddv and 3cve. denote the experimental structures used for assembling the full model The full length of the coiled-coil in the tetramer spans approximately 478A. **Figure S10:** All atom RMSD values calculated for the five parallel 200 ns molecular dynamics runs. **Figure S11:** The predicted model of the dimeric state of Homer1 using AlphaFold2 (above) The predicted mdel of the tetrameric state of Homer1 using AlphaFold3 (below). **Figure S12:** Characteristic dynamics of the Homer1 dimer/tetramer. **Figure S13:** Intra- and interchain interaction of the P-motif to the EVH1 domain. Intrachain interaction was modeled based on PDB:1ddv, for the interchain interaction our tetramer model was modified. In both cases Modeler from Chimera was used.